



# Estimating regional-scale daytime net surface radiation in cloudless skies from GEO-LEO satellite observations using data fusion approach

DHWANILNATH GHAREKHAN<sup>1,\*</sup> , RAHUL NIGAM<sup>2</sup>, BIMAL K BHATTACHARYA<sup>2</sup>,  
DEVANSH DESAI<sup>3,4</sup> and PARUL PATEL<sup>1</sup>

<sup>1</sup>Civil Department, Institute of Technology, Nirma University, Ahmedabad 382 481, Gujarat, India.

<sup>2</sup>Biological and Planetary Science and Applications Group, Space Application Center, ISRO, Ahmedabad 380 015, Gujarat, India.

<sup>3</sup>Department of Physics, Electronics and Space Science, Gujarat University, Ahmedabad 380 009, Gujarat, India.

<sup>4</sup>Department of Physics, Silver Oak Institute of Science, Silver Oak University, Ahmedabad 382 481, Gujarat, India.

\*Corresponding author. e-mail: dhwanilnath@gmail.com

MS received 20 November 2020; revised 10 November 2021; accepted 11 November 2021

Net surface radiation ( $R_n$ ) at earth surface comprises of outgoing and incoming components of longwave and shortwave radiation fluxes at the surface. This influences energy and mass exchange over earth surface at sub-daily, seasonal and annual time scales. This is a critical component for land surface models which characterize climatic, ecological and biological processes. Measured net radiation datasets are rarely available and can be subjected to errors and high uncertainties due to equipment malfunctions and failure. In this study, a regional-scale model is developed and implemented to estimate the net surface radiation fluxes over Indian landmass under cloudless sky conditions using the data from an Indian Geostationary (GEO) Meteorological satellite (INSAT 3D) and polar-orbiting (LEO) MODIS-Aqua for daytime conditions. The estimates were evaluated over a 6-month period (Nov 2019–Apr 2020) during winter and summer months, at three *in situ* measurement sites, located in cropland and grassland. The results showed a correlation of 0.86 between satellite-based  $R_n$  estimates and *in situ* measurements with a root mean square error (RMSE) of 40.4 W m<sup>-2</sup> (4.6% of measured mean) and a mean absolute error (MAE) of 5.6% of measured mean. The modelled estimates were compared with NCEP (National Center for Environmental Protection) reanalysis global surface radiation estimates diurnally. The NCEP model tends to under- or over-estimate during the study time period especially in the month of January.

**Keywords.** Net surface radiation; cloudless sky; INSAT; MODIS.

## 1. Introduction

Essential climate variables (ECV) are a group of linked variables (physical, chemical, biological), which collectively provide statistical and empirical evidence for understanding, predicting and modelling the earth's climate (Bojinski *et al.* 2014). The surface radiation (energy) budget, expressed in

terms of net radiation, is an ECV within the earth-atmosphere system. It is a fundamental quantity and component of the surface that modulates earth surface processes within the climate system. Net surface radiation ( $R_n$ ) surface comprises of incoming shortwave and outgoing longwave components of radiation fluxes at the surface. This influences energy and mass exchange over earth surface at

sub-daily, seasonal and annual time scales. This is a critical component for land surface models which characterize climatic, ecological and biological processes. Solar radiation flux is received at earth surface in shortwave region (0.3–3  $\mu\text{m}$ ) of electromagnetic wavelength after it passes through the Top Of the Atmosphere (TOA) and reaches the surface after interaction with various atmospheric constituents. The shortwave travels back into space through reflection or scattering by clouds, aerosols or the earth's surface and remaining amount is received at earth's surface. Thermal radiation in the longwave region (3–100  $\mu\text{m}$ ) is emitted by the surface and the atmosphere. Net radiation can be segregated into two distinctive zones: (i) net radiation flux at TOA and (ii) net surface radiation flux (hereafter denoted as  $R_n$ ). The earth radiation budget (ERB at TOA) describes the overall balance between the incoming shortwave energy flux from the Sun, reflected shortwave flux from Earth, the incoming longwave flux from air and sky, and outgoing longwave radiation from the surface. Any perturbation in the radiation budget at TOA causes positive or negative radiative forcing of the climate system (Dewitte and Clerbaux 2017). Net surface radiation ( $R_n$ ) is one of the major areas of focus of the earth-atmosphere system as it is responsible for all types of energy and mass exchange processes between earth surface and within the atmospheric boundary layer. The daytime  $R_n$  is essential to model various terrestrial eco-physiological processes such as evapotranspiration and photosynthesis over agro-ecosystems and natural ecosystems (Wei *et al.* 2018). The  $R_n$  is the sum of net surface shortwave ( $R_{ns}$ ) and net surface longwave ( $R_{nl}$ ) radiation fluxes (García *et al.* 2007).

One of the key uncertainties in site-specific evaluation of land surface energy balance, hydrological or ecological models stems from the lack of availability of systematic and continuous records of net radiation flux measurements, even at measuring stations where other key meteorological variables are measured (Abramowitz *et al.* 2012). Since 1950s, there have been numerous empirical models developed by scientists to estimate the net radiation flux components (Carmona *et al.* 2014). The studies focus on derivation of either net radiation or its individual components. These are location- and condition-specific and can lack practical applicability and scalability (Zhang *et al.* 2017). The simulations of global scaled General Circulation Models (GCM)

of 38 different models used in CIMP5 (Coupled Model Intercomparison Project 5) as well as satellite-based models to estimate radiation fluxes, were compared by Wild *et al.* (2019). The authors identified that radiation fluxes vary significantly during cloudless and cloudy sky conditions (Wild *et al.* 2019). Regional estimation models tend to be more precise at levels of agro-climatic zones and sub-zone. However, little attention had been given to regional estimations (Jones *et al.* 2017). Daily net surface radiation estimates are derived through LEO (Low Earth Orbiting) satellites such as MODIS (Moderate Resolution Imaging Spectroradiometer) (Verma *et al.* 2016). Regional estimation of daily  $R_n$  from LEO satellites generally uses a maximum of four observations from TERRA and AQUA during day and night time. These use of land surface parameters such as albedo, land surface temperature, land cover-based surface emissivity at finer resolution (500–1000 m) along with external inputs of coarser resolution ( $\sim 50$  km) modelled or reanalysis fields on incoming shortwave radiation flux and air temperature. On the other hand, geostationary (GEO) meteorological satellite provides observations at 15–30 min intervals throughout the day. This enables to compute instantaneous, diurnal and daily integral (Bhattacharya *et al.* 2009) of surface insolation (INS) as well as land surface temperature ( $T_s$ ) (Pandya *et al.* 2011) at less than 5 km resolution. Therefore, the combination of finer resolution less time-dynamic land surface variables such as land albedo and emissivity from LEO platform along with highly dynamic variables such as surface insolation and  $T_s$  at diurnal time scale from GEO platform can provide practical insight into regional-scale variability of  $R_n$  estimates. Net radiation approaches are higher km grid scale even for global estimates. Fusion approaches require higher temporal resolutions and more varied number of parameters. Renzullo *et al.* (2008) provided a 'multiple constraints' model-data fusion (MCMDF) scheme which was integrating AMSR-E (Advanced Microwave Scanning Radiometer for EOS – Earth Observation Satellite) soil moisture content (SMC) along with MODIS land surface temperature ( $T_s$ ) datasets that were coupled for a biophysical model of surface moisture and energy budgets for savannahs of over the northern Australian region (Renzullo *et al.* 2008). The results were compared with MODIS ET (evapotranspiration) and

thermal products as a validation which provided a strong agreement.

However, GEO-LEO data fusion approaches are sparsely used for net radiation estimates especially on a country scale (Cammalleri *et al.* 2013). Very few site-specific studies have provided evidence in the estimation of  $R_n$  at an hourly or half-hourly interval on a regional scale (Long *et al.* 2010). With better spatial-temporal availability, satellite-based products will help in understanding the inter- and intra-seasonal variability and atmospheric circulation pattern. In this study, our aim is to develop a unified model, that is capable of estimating  $R_n$  and its radiative fluxes under all-sky conditions. For example, one of the  $R_n$  components (incoming longwave radiation flux) has been derived using machine learning approaches under cloudy-sky conditions (Gharekhan *et al.* 2021). The current study presents (i) a model framework which estimates regional-scale diurnal  $R_n$  over the Indian landmass under cloudless conditions during daytime using GEO-LEO satellite data and (ii) validation of satellite-based  $R_n$  estimates over different agro-climatic settings with respect to *in situ* measurements and reanalysis fields.

## 2. Study region and data used

The study region comprises of Indian subcontinent spanned over 68.15°–97.2°E and 8.06°–37.1°N. It comprises of 15 broad agro-climatic zones identified by the Planning Commission in 1988 based on climatic conditions and suitability of crops which include solar radiation, rainfall, elevation, soil and others (Chattopadhyay *et al.* 2019). Different products from operational Indian geostationary (GEO) meteorological satellite (INSAT 3D) and polar orbiting (LEO) satellite (MODIS Aqua) were used for regional-scale estimation of  $R_n$ . The *in-situ* measurements of diurnal  $R_n$  at selected flux tower

sites in agro-ecosystem and grassland ecosystem were used for the evaluation of satellite-based estimates. The regional-scale inputs for  $R_n$  estimation are given in table 1.

Surface insolation [3DIMG\_L2C\_INS] is a second-level data product which provides the incoming solar radiation reaching at surface, estimated from the Indian GEO satellite, INSAT-3D, at every half-an-hour at 5 km spatial resolution (ISRO 2019) using a spectrally integrated cloudless-sky model and three-layer cloudy-sky model (Bhattacharya *et al.* 2009) using visible (0.52–0.72  $\mu\text{m}$ ), thermal IR (Infrared) (10.2–12.5  $\mu\text{m}$ ) and water vapour bands (6.5–7.0  $\mu\text{m}$ ) of INSAT 3D ‘Imager’.

The land surface temperature ( $T_s$ ) [3DIMG\_LST\_L2B] is retrieved through split-window algorithm tuned for INSAT 3D ‘Imager’ split-thermal infrared (TIR) bands (10.2–11.2  $\mu\text{m}$  for TIR1 and 11.5–12.5  $\mu\text{m}$  for TIR2) at every half-an-hour interval at 4 km spatial resolution (Pandya *et al.* 2011). Both diurnal daytime  $SW_{in}$  and  $T_s$  are generated through an automated processing chain and available through MOSDAC ([www.mosdac.gov.in](http://www.mosdac.gov.in)) portal for the user community.

The albedo ( $\alpha$ ) [MCD43C3] is a level-3 MODIS terra-aqua combined daily averaged global product produced at 0.05° grid resolution. MCD43C3 Version 6 Bidirectional reflectance distribution function and Albedo (BRDF/Albedo) dataset is produced daily using 16 days of Terra and Aqua MODIS data at a 0.05° resolution (5.6 km at the equator) aggregated climate modelling grid (CMG) (NASA and Schaaf 2019).

Surface emissivity [ $\epsilon_s$ ] was acquired using month averaged surface emissivity product [MOD11C3]. In the day–night algorithm, surface emissivity is retrieved from pairs of day and night MODIS observations in seven TIR bands (NASA and Frazier 2019), which was later combined with same month 10-year historical datasets, thus having

Table 1. Satellite-based and gridded weather forecast products used for estimation of net surface radiation over Indian Landmass in cloudless skies.

Regional-scale inputs	Unit	Spatial resolution	Source	Data code	Temporal resolution
Surface insolation ( $SW_{in}$ )	$\text{W m}^{-2}$	5 km	INSAT 3D	3DIMG_L2C_INS	30 min
Albedo ( $\alpha$ )		0.05° grid (5.5 km)	MODIS Aqua	MCD43C3	Daily
Air temperature ( $T_a$ )	K	5 km	WRF model	Ta_2	3 hours
Surface emissivity ( $\epsilon_s$ )		0.05° grid (5.5 km)	MODIS	MOD11C3	10-year monthly mean
Land surface temperature ( $T_s$ )	K	5 km	INSAT 3D	3DIMG_LST_L2B	30 min

more reliable information over the region at global scale  $0.05^\circ$  resolution. Inaccuracy in the estimation of surface emissivity can cause errors in the net longwave flux estimates at the surface (Hartmann 2016). To overcome this, MODIS provides monthly averaged emissivity measurement over the globe with  $0.05^\circ$  grid resolution and a 10-year mean (2010–2018) was generated for each month. Regional subsets of MODIS albedo and surface emissivity products were used for  $R_n$  estimation.

A reanalysis gridded climate dataset on net shortwave and net longwave fluxes in cloudless skies is provided by NOAA/OAR/ESRL PSL (<https://psl.noaa.gov/>), Boulder, Colorado, USA, on a global level of surface fluxes. The NCEP provides net shortwave and net longwave radiation flux estimates four times per day as well as daily average globally at a spatial resolution of  $2^\circ$  Gaussian grid (roughly 220 km spatial resolution) (Kalnay *et al.* 1996). The 4-time daily estimates were averaged to derive a daytime daily net radiation estimate. The daily daytime fluxes were averaged for 15 days for comparison.

The reanalysis product ERA5 (ERA5: Fifth generation of ECMWF atmospheric reanalyses of the global climate) provided by the Copernicus Climate Change Service (C3S) was taken into comparison. This is a replacement on the ERA-Interim which has been discontinued since October 2019. The ERA5 provides monthly as well as hourly estimates of different atmospheric and meteorological parameters. It provides separate net shortwave and longwave fluxes at an hourly interval throughout the day which can be added to derive  $R_n$  during the daytime. ERA5 provides a higher spatial resolution of 31 km as opposed to its predecessor ERA-Interim (8 km) (Hersbach *et al.* 2020). The dataset can be accessed at <https://cds.climate.copernicus.eu/cdsapp#!/home> (CDS 2017).

Weather Research and Forecast Model (WRF) is a numerical model adapted for the generation of important weather variables for short-range forecasting. The model serves for a large range of meteorological applications across the Indian landmass. WRF derives simulations based on actual atmospheric conditions (i.e., from observations and analyses) or can be simulated for idealized conditions. It offers operational forecasting a flexible computationally-efficient platform, while highlighting the recent advances in physics, numeric and data assimilation contributed by developers from the expansive research community (Kumar *et al.* 2012). It is a limited area,

non-hydrostatic, primitive equation model which is operational for multiple and diverse physical parameterization schemes. The current model employs Arakawa C-grid staggering for the horizontal grid and a fully compressible system of equations. The terrain following hydrostatic pressure coordinated with vertical grid stretching was followed in vertical. The time-split integration uses 3<sup>rd</sup> order Runge–Kutta scheme with a smaller time step for acoustic and gravity wave modes (Kumar *et al.* 2011). The regular WRF model output for different surface and meteorological parameters is generated by AOSG (Atmospheric and Oceanic Science Group), SAC (Space Application Centre), ISRO (Indian Space Research Organisation) after assimilation of satellite radiances (Kumar *et al.* 2012). The WRF model has been customized to provide short-range forecasts at 5 km spatial resolution at 3-hr intervals over Indian subcontinent where data assimilation from Indian and global satellite observations to the model has been made operational at SAC (Space Applications Centre), ISRO (Indian Space Research Organisation). The model has been assessed and validated with global products available in different studies that provided a strong correlation for radiative and soil fluxes over different resolutions diurnally and with respect to *in situ* measurements from micrometeorological towers (Kumar *et al.* 2016).

*In situ* measurements on diurnal  $R_n$  were recorded using net radiometer at 30 min intervals. These *in situ* datasets were recorded during the INCOMPASS (INteraction of Convective Organization and Monsoon Precipitation, Atmospheric Surface and Sea) campaign under Indo-UK collaborative project to study monsoon dynamics under different agro-climatic regions with ground-based high-response sensors and aerial flight measurements (Turner *et al.* 2019). Under this project, net radiometers (Kipps and Zonen CNR4) were installed along with meteorological assembly. The radiation sensor is a 4-component net radiometer that measures incoming and outgoing shortwave and longwave radiation fluxes. This is a four-component net radiometer that measures incoming ( $SW_{in}$ ) and outgoing ( $SW_{out}$ ) shortwave, incoming ( $LW_{in}$ ) and outgoing ( $LW_{out}$ ) longwave radiation fluxes with uncertainty in daily mean of less than 10% (at 95% confidence level) for each component (Rubel and Kottke 2011). The sensors have a high response time of less than 18 sec, with a sensitivity of measurement within  $5\text{--}20 \mu\text{V W}^{-1} \text{m}^{-2}$  (Zonen

Table 2. Agro-climatic characteristics of evaluation sites.

Site	Lat. (°N)	Long. (°E)	Agro-climatic sub-zone	Climate and vegetation	Mean annual $T_a$ (°C)	Annual $P$ (mm) (CV (%))
Jaisalmer (Rajasthan)	26.99°	71.34°	Arid western zone	Arid grassland	$T_{max}$ : 25–40 $T_{min}$ : 8–25	100–300 (56)
Nawagam (Gujarat)	22.8°	72.57°	Middle Gujarat zone	Semi-arid cropland	$T_{max}$ : 29–39 $T_{min}$ : 9–25	700–850 (36)
Samastipur (Bihar)	26°	85.67°	Northwest alluvial plain zone	Humid-subtropical cropland	$T_{max}$ : 23–29 $T_{min}$ : 10–20	900–1200 (17)

$T_a$ : air temperature;  $T_{max}$ : daily maximum temperature during the period observed by Ghosh (1991);  $T_{min}$ : daily minimum temperature during the observation period of 1990;  $P$ : rainfall (mm) measured using rain gauge at EC site during the observation period of 1990 (Ghosh 1991). The period during winter and summer months (1 Nov 2019–Apr 2020) was chosen for validation of satellite-based estimates of  $R_n$  for cloudless skies. Their bias correction is later depicted in table 3.

2019). The concurrent measurements on relative humidity and air temperature were recorded using other pre-installed sensors. Presently, under INCOMPASS, the measurement systems installed at three different homogeneous agro-ecosystem sites are at (1) Jaisalmer, Rajasthan, (2) Nawagam, Gujarat, and (3) Samastipur, Bihar which were used as a reference for evaluation of satellite-based  $R_n$  estimates. Their climatic characteristics are explained in table 2.

### 3. Methodology

#### 3.1 Cloudless sky daytime net surface radiation model

Net surface radiation ( $R_n$ ) flux is the sum of net shortwave ( $R_{ns}$ ) and net longwave radiation ( $R_{nl}$ )

$$R_n = R_{ns} + R_{nl}, \quad (1)$$

$$R_{ns} = SW_{in} - SW_{out}, \quad (2)$$

$$R_{ns} = SW_{in}(1 - \alpha), \quad (3)$$

where  $SW_{in}$ : incoming shortwave radiation: Insolation [ $W m^{-2}$ ],  $SW_{out}$ : outgoing shortwave radiation [ $W m^{-2}$ ],  $\alpha$  = Albedo [unit less]. The  $R_{nl}$  is the difference between incoming ( $LW_{in}$ ) and outgoing ( $LW_{out}$ ) longwave radiation fluxes. The  $LW_{in}$  can be expressed as:

$$LW_{in} = \epsilon_a \sigma T_a^4, \quad (4)$$

where  $T_a$  is the air temperature (K),  $\epsilon_a$  is effective clear-sky atmospheric emissivity,  $\sigma = 5.6 \times 10^{-8}$  ( $W m^{-2} K^4$ ) is Stephen Boltzmann's Constant. The  $\epsilon_a$  over a region cannot be directly measured. Bastiaanssen (1995) proposed an empirical

relationship between incoming solar irradiance at earth surface through  $SW_{in}$  and the solar irradiance received at the top of the atmosphere aka extra-terrestrial solar radiation ( $R_{ext}$ ) flux (Bastiaanssen 1995):

$$\epsilon_a = 0.85 - \ln T_{sw}^{0.09}, \quad (5)$$

where

$$T_{sw} = 1 - \frac{SW_{in}}{R_{ext}}, \quad (6)$$

$$R_{ext} = G_{sc} * \cos\left(\frac{\pi}{180} SZA\right) * e, \quad (7)$$

where  $G_{sc}$  is the solar constant, i.e.,  $1367 W m^{-2}$ ,  $SZA$  is Solar Zenith Angle,  $SW_{in}$  is incoming shortwave radiation ( $W m^{-2}$ ),  $e$  is the eccentricity of surface interaction that includes scattering, emission and absorption of energy based on sun–earth distance-correction factor,  $T_{sw}$  is defined as atmospheric transmissivity, a ratio of all-sky mean downwelling SW flux to the mean of SW flux in cloud-free sky widely used in both observational modelling and GSMs (Qian *et al.* 2012). The energy emitted by the surface in the infrared region (4–100  $\mu m$ ) can be defined as outgoing longwave radiation ( $LW_{out}$ ). This can be estimated from surface emissivity ( $\epsilon_s$ ) and land surface temperature ( $T_s$ ).

$$LW_{out} = \epsilon_s \sigma T_s^4. \quad (8)$$

Therefore,  $R_n$  can be expressed as:

$$R_n = INS(1 + \alpha) + \left[ \left( 0.85 - \ln \left[ \frac{SW_{in}}{R_{ext}} \right]_{sw}^{0.09} \right) \sigma T_a^4 \right] + \epsilon_s \sigma T_s^4. \quad (9)$$

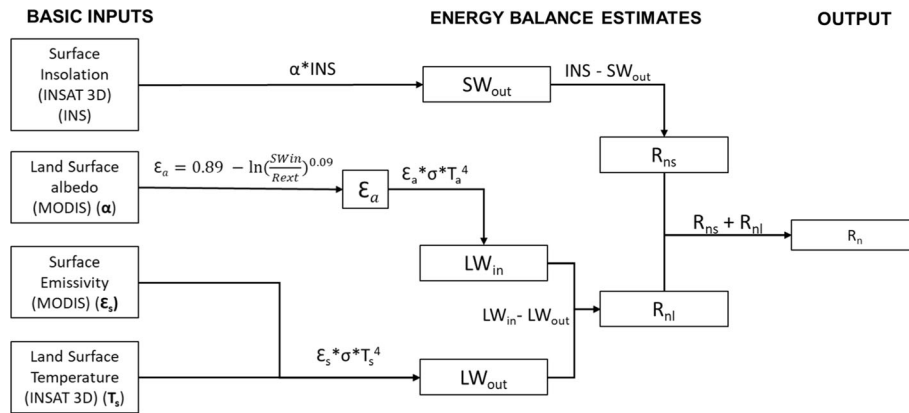


Figure 1. Methodology flow to derive  $R_n$  over Indian landmass under cloudless sky conditions.

### 3.2 Data fusion approach for regional-scale implementation of model

Data fusion approaches process information with the adaptation of technology that can and is being used to analyse, synthesize, simulate and predict several observation measurements acquired from multiple satellites in time sequence under specific criteria. This facilitates to complete the required decision-making, evaluation tasks and provides estimates of other parameters (Zhang *et al.* 2013). This approach tends to rescale multisource to a required spatial resolution. These approaches provide high applicability in the analysis of ocean and meteorological observation datasets, especially for parameters that cannot be directly measured on large-scale regions (Wei *et al.* 2019). The present study adapts a data fusion approach for operational implementation of regional-scale  $R_n$  model. The model framework is presented below through this flow chart in figure 1.

The strength of the proposed methodology is that it considers the advantages of satellite remote sensing-based products from both GEO and LEO platforms and short-range gridded air temperature forecast from operational NWP (Numerical Weather Prediction) model which can be used to derive  $R_n$  at high temporal interval without dependence on *in situ* measurements. The regional-scale  $R_n$  was computed at an interval of 30 min during daytime hours.

## 4. Results and validation

### 4.1 Sensitivity of cloudless-sky $R_n$ to land surface and meteorological inputs

Quantifying the sensitivity of  $R_n$  estimates to variability or uncertainty associated with input

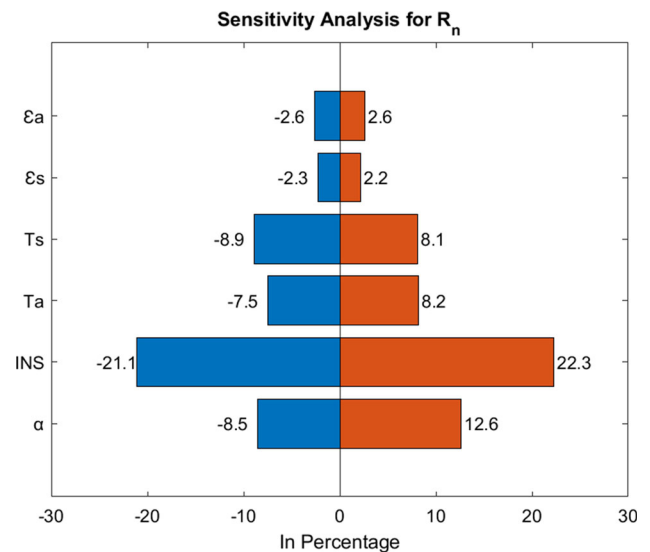


Figure 2. One-dimensional sensitivity analysis of  $R_n$  to land surface and meteorological inputs.

variables is essential. Identifying the influence of each parameter for the output is necessary. One-dimensional (1D) is a linear approach to observe these influences. 1D sensitivity analysis was carried out using change in different input levels from their mean to evaluate the impact on  $R_n$  estimates (depicted in figure 2).

In 1D sensitivity analysis, one input variable was changed within its theoretical or practical range while keeping other inputs constant. The input variables were normally changed from its fixed or central value up to  $\pm 50\%$  (Nigam *et al.* 2014) as per the characteristic of input variable. However, due to the nature and range of the input variables, individual scales were adapted. The detailed values can be found in Appendix, table A1. The sensitivity analysis showed that change in input variable albedo ( $\alpha$ ) from its mean

value 0.25 to  $\pm 1.5\%$  lead to  $\pm 10\%$  change in instantaneous  $R_n$ . The change in land surface emissivity ( $\epsilon_s$ ) of the order of  $\pm 0.03\%$  led to 2% deviation in  $R_n$ . On the other hand, meteorological and land surface variables such as temperature ( $T_a$  and  $T_s$ ) or surface insolation ( $SW_{in}$ ) also influence  $R_n$  which showed less percent change in  $R_n$  as compared to  $\epsilon_s$  and  $\alpha$ . Deviation of  $\pm 3^\circ$  in  $T_a$  and  $T_s$  led to approximately 5% change in  $R_n$ . Further, a change in surface insolation of the order of 2–4% alters the overall  $R_n$  with a change of 1–2%.

#### 4.2 Evaluation of satellite-based daytime $R_n$ estimates

The diurnal satellite-based daytime  $R_n$  estimates between 8 and 17 hrs were compared with *in situ* measured  $R_n$  in semi-arid sites at cropland in Nawagam, Gujarat and desert grassland in Chandan, Jaisalmer at half-an-hour interval for selected dates and cloudless-sky occurrences at 15 days' interval during Nov 2019–Apr 2020 (figure 3). This showed a close match between satellite-based  $R_n$  estimates and measurements on selected dates with RMSE varying from 2.4 ( $9.5 \text{ W m}^{-2}$ ) to 21.9% ( $35.9 \text{ W m}^{-2}$ ) and MAE from 2.8 ( $11.1 \text{ W m}^{-2}$ ) to 14.1% ( $51.3 \text{ W m}^{-2}$ ) of measured mean with correlation coefficient in the range of 0.83–0.99. The deviations of  $R_n$  estimate from measurements were found to be more at early and late morning hours in the order of 7.7%. While satellite-based  $R_n$  flux estimates were found to be smooth, the measured  $R_n$  fluxes are less smooth in nature in some cases. Satellite observations are instantaneous while the *in-situ* measurements have been averaged to 30 min. Moreover, there is a possibility of presence of thin clouds just over tower footprint of less than  $1 \text{ km}^2$  at any or multiple instances within 30 min but not entirely occupying the  $16 \text{ km}^2$  corresponding to pixel footprint at the time of instantaneous observations from INSAT 3D 'Imager'. In addition to that, wind turbulence impact on thermal infrared emittance plays a dominant role when measurement footprint is of few meters and the effect fades out with coarser measurement footprint. However, sudden change in wind turbulence may show up effect on thermal emittance and thereby  $R_n$  measurements even at coarser scale around  $1 \text{ km}^2$ . But the turbulence effects are minimal at the footprint of INSAT 3D 'Imager'. These are the reasons for getting less smooth

diurnal curve of 30 min average measured fluxes but not in the case of satellite estimated instantaneous fluxes.

The diurnal plots between modelled and *in situ* measurements at fortnightly interval over Jaisalmer, Nawagam and Samastipur are shown in figure 3 with their statistical performance in Appendix, table A2.

The correlation consistently showed a strong agreement of the modelled estimates with *in-situ* measurements. Jaisalmer showed only 5.7% error in January, while it increased to 7.4% in the month of March while in April, errors could not be assessed due to lack of datasets. Similarly, Nawagam had a lower error in January (6.5%) as against March (8.2%) while it dropped further in April (4.2%). The lack of measurements in November and December signifies the presence of clouds/fog which restrict the observations of the surface (Kesarwani *et al.* 2018). From January to April, error increased due to the rise in aerosol in atmosphere (Yoon *et al.* 2014). The climatology of 8-day MODIS AOD at  $1^\circ$  grid resolution was used for operation generation of surface insolation product in cloudless skies for cloudless-flagged pixels of INSAT 3D imager data. Deviation of AOD from climatic mean tends to increase during March to May period especially in Jaisalmer and Nawagam regions due to sporadic dust events (Masoom *et al.* 2020). Moreover, the coarse resolution ( $1^\circ$ ) product is not able to quantify sub-grid variability of AOD due to increased aerosol loading (Roelofs 2012). These might lead to increasing deviations in insolation product and measurements. The higher uncertainty of AOD especially over brighter regions (snow, ice, desert and barren lands) can be a factor for higher errors of surface insolation under aerosol loaded skies (Mishra *et al.* 2014). While the correlation was high, the model still tends to overestimate over desert grassland in Jaisalmer and underestimate in agriculture landscape at Nawagam especially during sunrise and sunset hours. The errors might have originated due to differences in temporal resolution of various satellite and WRF-based inputs. While  $SW_{in}$ ,  $R_{ext}$  vary at each 30-min interval, there are a few inputs that are not estimated at such a high temporal resolution which might also propagate errors in the  $R_n$  model estimates. The variable such as surface emissivity is assumed as static input change with each computation over a long temporal duration (more than a month). The albedo serves as semi-static input because it does not change with every

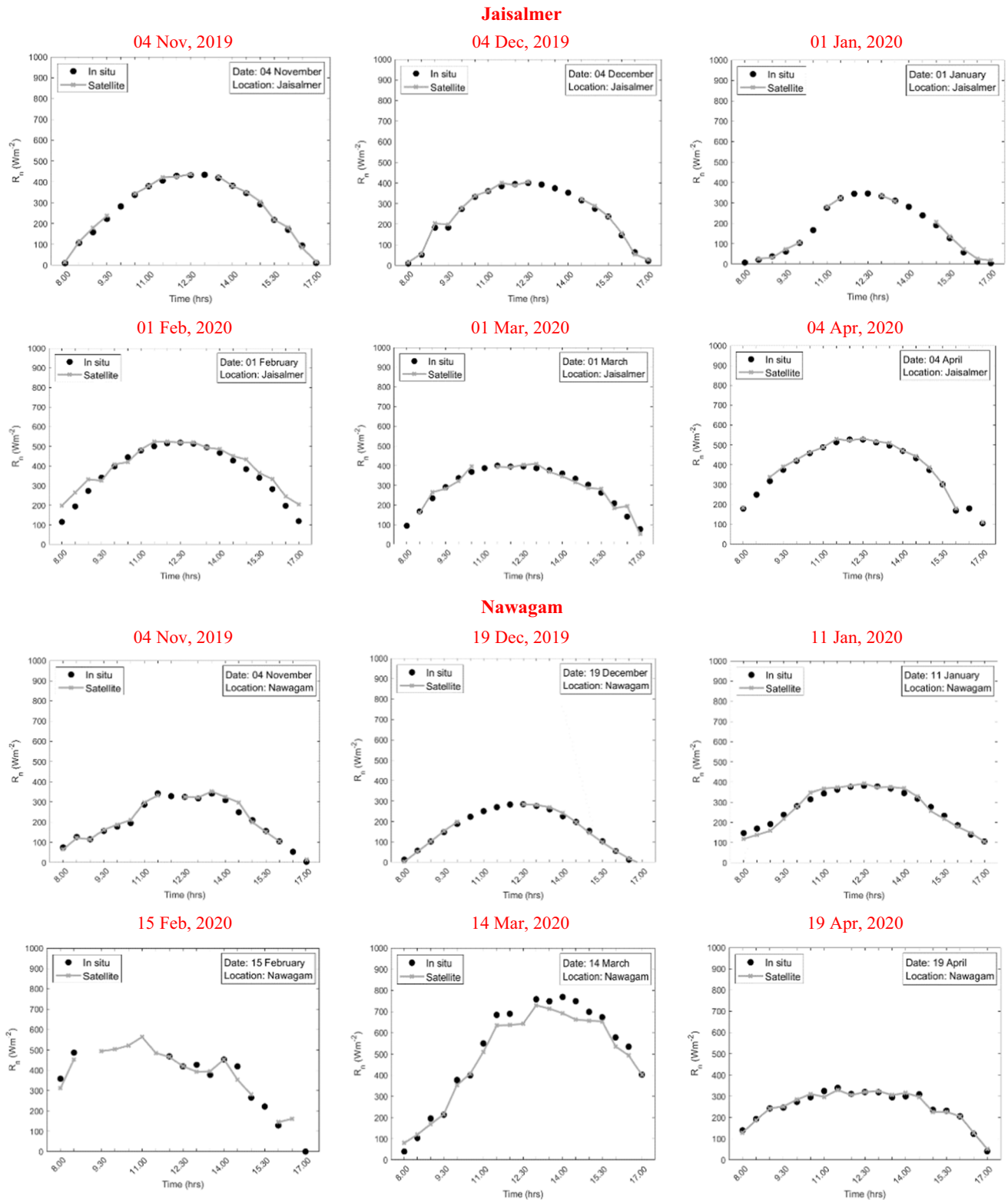


Figure 3. Diurnal daytime pattern of modelled and measured  $R_n$  at Jaisalmer, Nawagam and Samastipur on selected cloudless dates during January–March, 2020. The x-axis represents the time (in hrs) and the y-axis depicts the  $R_n$  (in  $W m^{-2}$ ).

computation but change after a specific time period within few days to a month.  $SW_{in}$  and  $T_s$  are the most dynamic inputs which change with 30 min

intervals. The WRF model forecasts  $T_a$  over the Indian landmass with a spatial resolution of 5 km at a temporal resolution of 3 hrs. All these lead to a

**Samastipur**

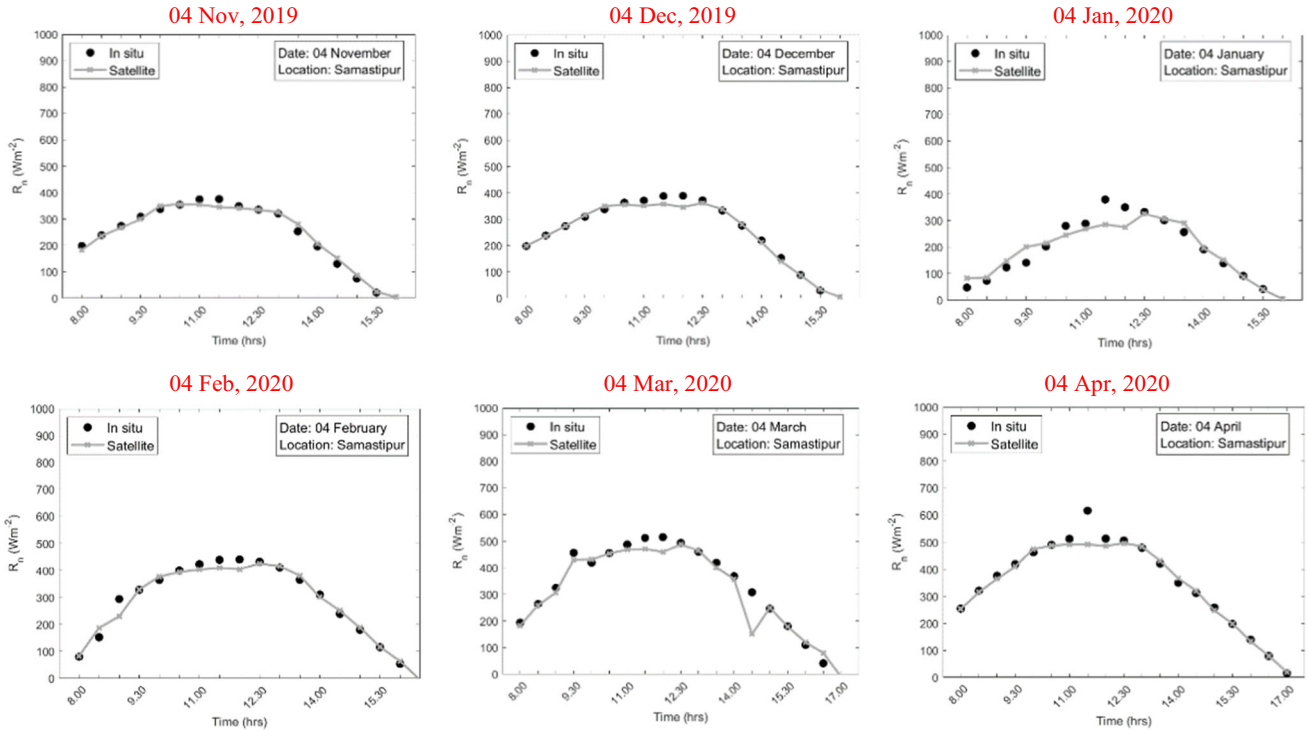


Figure 3. (Continued.)

confounding effect that leads to error in the satellite estimates of  $R_n$ .

The  $T$ -test was performed for validation of the model with respect to *in situ* measurements (figure 4). The probability distribution function (PDF) curve showed a symmetric fit to the dataset with little positive skewness. The statistical significance and the degree of correlation of the estimates (no. of points ( $n$ ) = 1524) with respect to measurements was tested at 95% confidence interval ( $\alpha = 0.05$ ) that produced acceptance rate lower than  $p \leq 0.001$  (actual  $p = 1.48E-7$ ) with mean ( $\mu$ ) of  $343.3 \text{ W m}^{-2}$  and standard deviation ( $\sigma$ ) of  $161.2 \text{ W m}^{-2}$ , indicating highly significant result as determined through paired  $T$ -test with a Pearson correlation coefficient ( $r = 0.88$ ).

Output of modelled estimates and *in situ* measurements under specific conditions do not always produce high performances and can have variations. These variations, i.e., bias errors between ground observations and modelled estimates can be due to imperfect conceptualization, discretization and spatial averaging within grid cells (Soriano *et al.* 2019). Bias corrections are the process of scaling modelled outputs in a way that can account for these systematics errors, thus improve their fitting to observations. There are several bias

correction models and linear or quadratic scaling is the most common approach used within empirical estimates as the errors are very sparse and can be specific under difficult situations (Moghim and Bras 2017).

$$R_{nb} = 4.31 * 10^{-4}(R_n^2) + 0.51(R_n) + 90.5 \quad (10)$$

where  $R_{nb}$  is bias corrected  $R_n$  [ $\text{W m}^{-2}$ ]. The validation plot (figure 5) of satellite-based  $R_n$  estimates on half-an-hourly basis and measurements for all the cloudless-sky occurrences showed high correlation coefficient ( $R^2 = 0.73$ ) and RMSE ( $90.1 \text{ W m}^{-2}$ ) of the order of 8.6% of measured mean (highlighted in table 3) for 1524 paired datasets. Since, there are differences between footprint of satellite-based  $R_n$  estimates ( $0.05^\circ$ ) and point measurements (few meters only) as well as differences in temporal frequency (half-an-hourly, three hourly, once daily) among spatial inputs for  $R_n$  estimates, a linear bias correction method was used to minimize the bias of  $R_n$  estimates. This has reduced the RMSE of satellite-based  $R_n$  estimates to 5.6% ( $40.4 \text{ W m}^{-2}$ ) of measured mean and increased the correlation coefficient ( $R^2 = 0.87$ ). Recently, Verma *et al.* (2016) estimated  $R_n$  on a global scale at 5 km spatial resolution from LEO platform only using MODIS Terra and Aqua

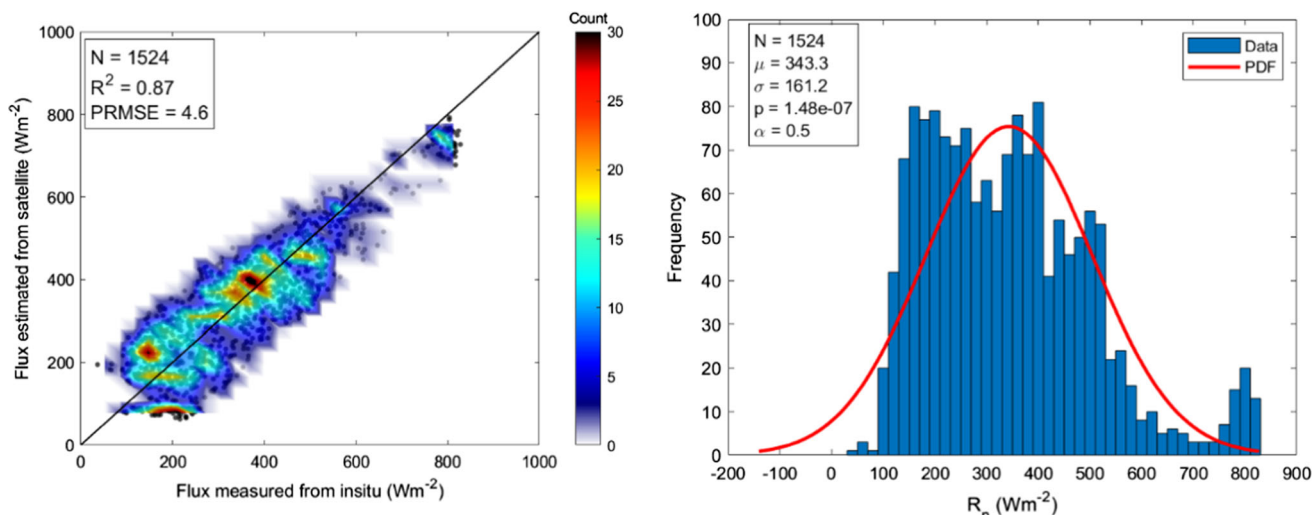


Figure 4. Scatter density plot (left) and probability distribution curve (right) between  $R_n$  flux from *in situ* measurements vs. estimates from satellite-based observations of cloudless-sky during 8 am to 5 pm for the period, 1 November to 19 April 2020 at three sites (Jaisalmer, Nawagam, Samastipur).

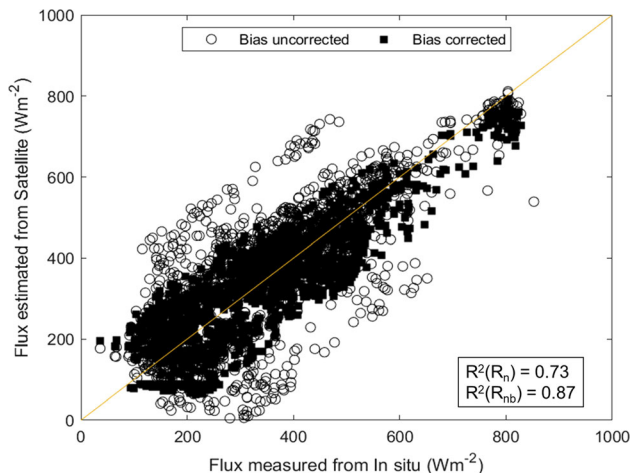


Figure 5. Validation plot of bias-corrected satellite-based  $R_n$  estimates and *in situ* measurements during 1 November 2019 to 19 April 2020.

Table 3. Statistical performance of bias-uncorrected and corrected model estimates.

Model	RMSE ( $W m^{-2}$ )	PRMSE (%)	$R^2$	MAE (%)
$R_n$	90.1	20.2	0.73	8.6
$R_{nb}$	40.4	4.6	0.87	5.6

Note:  $R_n$  is model estimated net radiation [ $W m^{-2}$ ] and  $R_{nb}$  is bias corrected [ $W m^{-2}$ ].

products and compared with *in situ* measurements from 154 sites from the FLUXNET and surface radiation budget network (SURFRAD) with correlation coefficient of 0.74 for boreal to 0.63 for

Mediterranean sites and at some specific regions as high as 0.9 (Verma *et al.* 2016). On a regional level, Wu *et al.* (2017) estimated  $R_n$  for the Heihe river basin in China and derived  $R_n$  for 12 months in the year 2008 and at four stations with different underlying surface type and acquired an  $R^2$  of 0.86. This approach was identification of cloud parameters using GEO satellite FY-2D, while MODIS 1D product provided a clear sky reflectance. The approach considered the ground-based estimates as a training input in regional scales within the Heihe river and using sunshine hours for net shortwave and FAO-56 method for deriving net longwave radiation (Wu *et al.* 2017). Other studies have also reported higher accuracies in regional hybrid models (Yang and Shang 2013).

The method which incorporates land-based measurements are limited for the specific site and the approach is needed to be tuned for different region estimates. Such hybrid ground-based models are region-specific and cannot provide large-scale estimates with high accuracies.

The reanalysis data over Jaisalmer, Nawagam and Samastipur (depicted in figure 6) were found to be close to the modelled  $R_n$  estimates from GEO-LEO satellites and both are slightly underperforming during the month of January. As compared to globally reported studies, the current model performance with spatial inputs is at par and even better than the global estimates as shown with the comparison with the NCEP reanalysis data. ERA5 provided near matching measurements in comparison with the NCEP and satellite

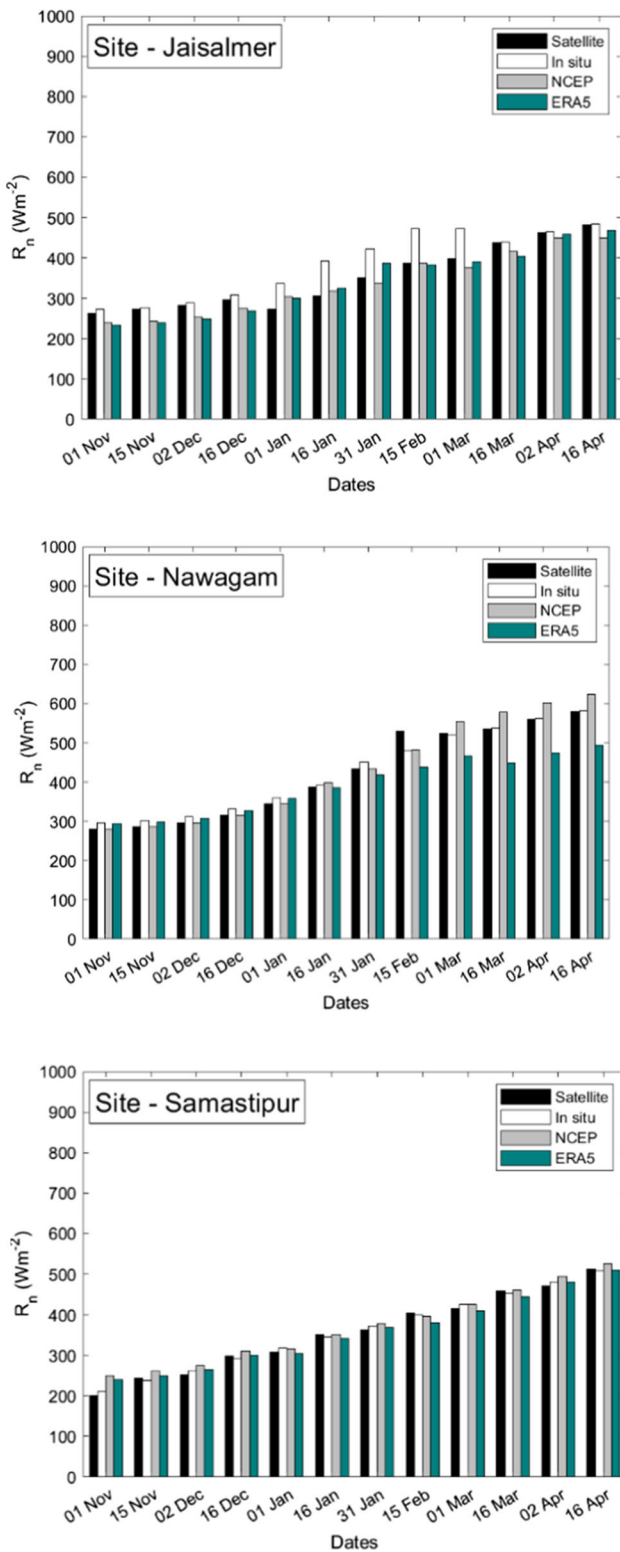


Figure 6. Daytime 15-day average net radiation comparison among satellite-based estimates, reanalysis and *in situ* measurements over Jaisalmer, Nawagam and Samastipur.

modelled  $R_n$ . Higher variation was observed during the month of March for both sites. The variations in  $R_n$  estimates across March and April are due to

the high presence of suspended aerosols that are prominent during the peak summer months over India, which ERA5 and other data sources are identifying. The overall 15-day averaged pattern in Samastipur showed a steady increase in the  $R_n$  estimates and measurements, a testament to the onset of summer months. The NCEP and ERA5 estimates were found to closely match with the *in-situ* measurements and satellite-based estimates in March and April. In the arid and semi-arid regions over Nawagam and Jaisalmer, respectively, ERA5 tends to underperform. This can be due to its coarser native resolution which might smoothen out the sub-grid variabilities. The  $R_n$  estimates obtained using data fusion approach with GEO-LEO satellite data showed overall good agreement with the *in situ*, NCEP and ERA5 measurements, despite having different native spatial resolutions or footprints.

Satellite-based estimates were scaled to the NCEP resolution and compared for the 19th February, 2020. The percentage difference on spatial scale between the two estimates was found to be very less of the order of 0.1–0.5% as shown in figure 7 with relatively higher difference in southern India. This shows close match of modelled  $R_n$  estimates from GEO-LEO satellites and reanalysis data over Indian landmass.

#### 4.3 Regional distribution of $R_n$ estimates in pre-monsoon months

The regional distribution of satellite-based  $R_n$  estimates over Indian landmass at 1530 IST on selected dates during November 2019–March 2020 are exemplified in figure 8. The blank regions symbolize overcast conditions from dust storm, clouds, etc. The shift in colour pattern depicts the change with months.

The oceanic winds flowing into India from the southwest through Indian Ocean lead to the formations and variabilities in the seasonal changes. The fortnightly images also highlight the path in which the net radiation estimates are gradually rising from the southwest direction (Backeberg *et al.* 2012). The East India Current defines the northward-flowing wind movement entering through the Bay of Bengal leading to the onset of monsoon and more cloud generation from February. McCreary *et al.* (1996) and few others reported that this is due to the wind stress induced on the east India coast region, which leads to a larger

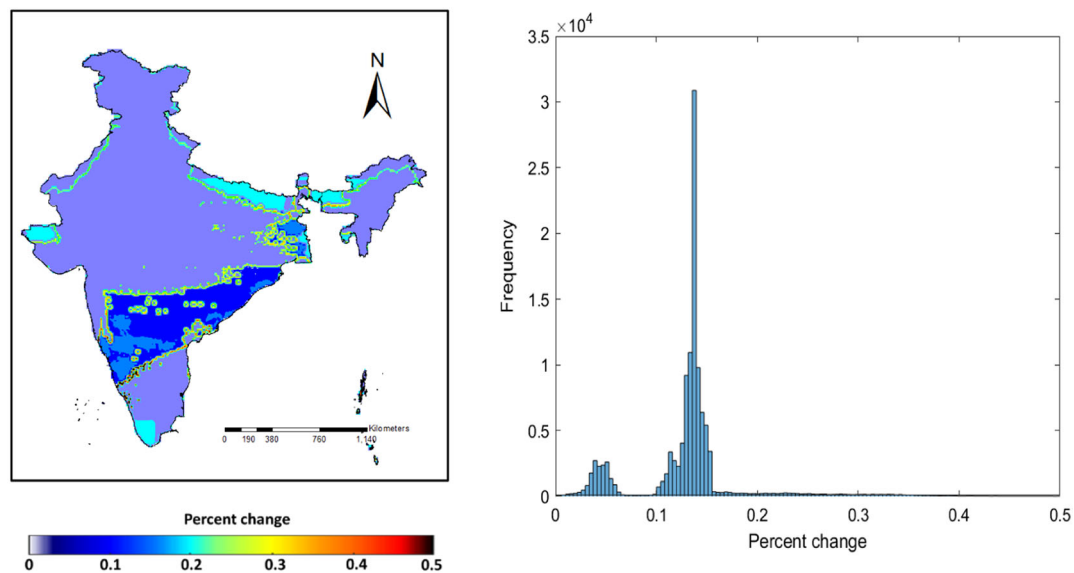


Figure 7. Histogram and spatial pattern of percent difference between 15-day daytime average net surface radiation estimates between ERA5 reanalysis fluxes and satellite-based estimates on the 19th of February, 2020.

onset of clouds from the month of February till October (McCreary *et al.* 1996). This is why the modelled images have more amount of missing measurements due to overcast clouds flowing towards India from the eastern coast near the Bay of Bengal. While during the months of November–December, the estimates could not be derived due to cloud perturbations, the north-eastern region showed  $R_n$  estimates in the range of  $300\text{--}350\text{ W m}^{-2}$  at the beginning of January. This increased to  $450\text{ W m}^{-2}$  within the span of 3 months due to the onset of summer and concomitant increase in surface insolation and reduction in net longwave radiation due to an increase in  $T_s$ .

The  $R_n$  histograms (figure 9) showed tetra-modal pattern during 1st fortnight of January and gradually shifts towards tri-modal pattern towards 1st fortnight of February. These showed largely bimodal pattern during second fortnight of February to second fortnight of March. Due to the limited satellite observations during the months of November, December and April, the histograms patterns are sparsely spread and donors highlight a Gaussian distribution. Despite all, the satellite-based estimates under cloudless skies provide a good agreement with *in situ* measurements. With different approaches for overcast conditions like  $LW_{in}$  estimation under cloudy skies combined with the clear-sky model,  $R_n$  estimation would be possible under all-sky conditions.

Higher number of modes could be due to differences in land surface phenological contrast and water management in different crop types over northern, southern, western and eastern India. These could lead to variability in both net shortwave and net longwave radiation flux. During peak growth stages which generally occur during late February to late March in India,  $R_n$  was mostly influenced by contrasting net shortwave radiation regime between northern and southern India that led to largely bimodal distribution. The monthly NDVI (normalized difference vegetation index) acquired from MODIS suggests decrement of vegetation vigour over India during the month of March, which shifts further during April (shown in figure 10). The histogram provides the spread of observations post-applying an agriculture mask and removing other pixels. The regional mean and median of satellite-based  $R_n$  estimates for Nov to Apr were found to vary within a large range of  $154\text{--}442$  and  $196\text{--}464\text{ W m}^{-2}$ , respectively increasing from November towards April (Appendix, table A3) while standard deviation was found to vary within  $66\text{--}115\text{ W m}^{-2}$ . This could be related to the change in extra-terrestrial radiation and eventually the change in insolation received on the surface over India with time from January to March where extensive decrease in atmospheric water vapour especially in the west and north-western parts of India occurred due to the onset of summer season. The flow of winds and the western disturbances originating over the Indian

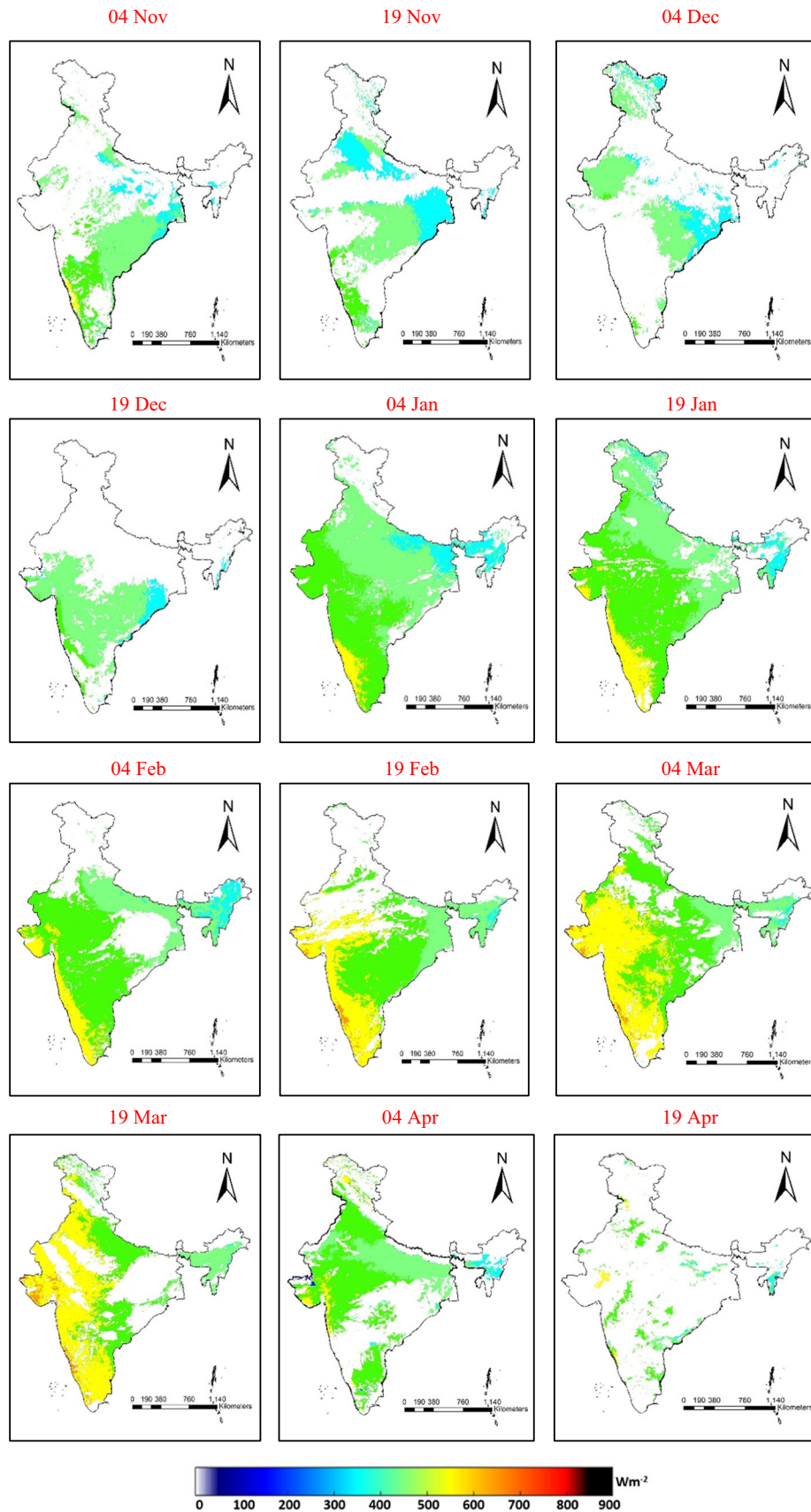


Figure 8. Regional-scale cloudless-sky  $R_n$  estimates at 1530 IST in each fortnight between Nov 2019 and Apr 2020 over Indian landmass.

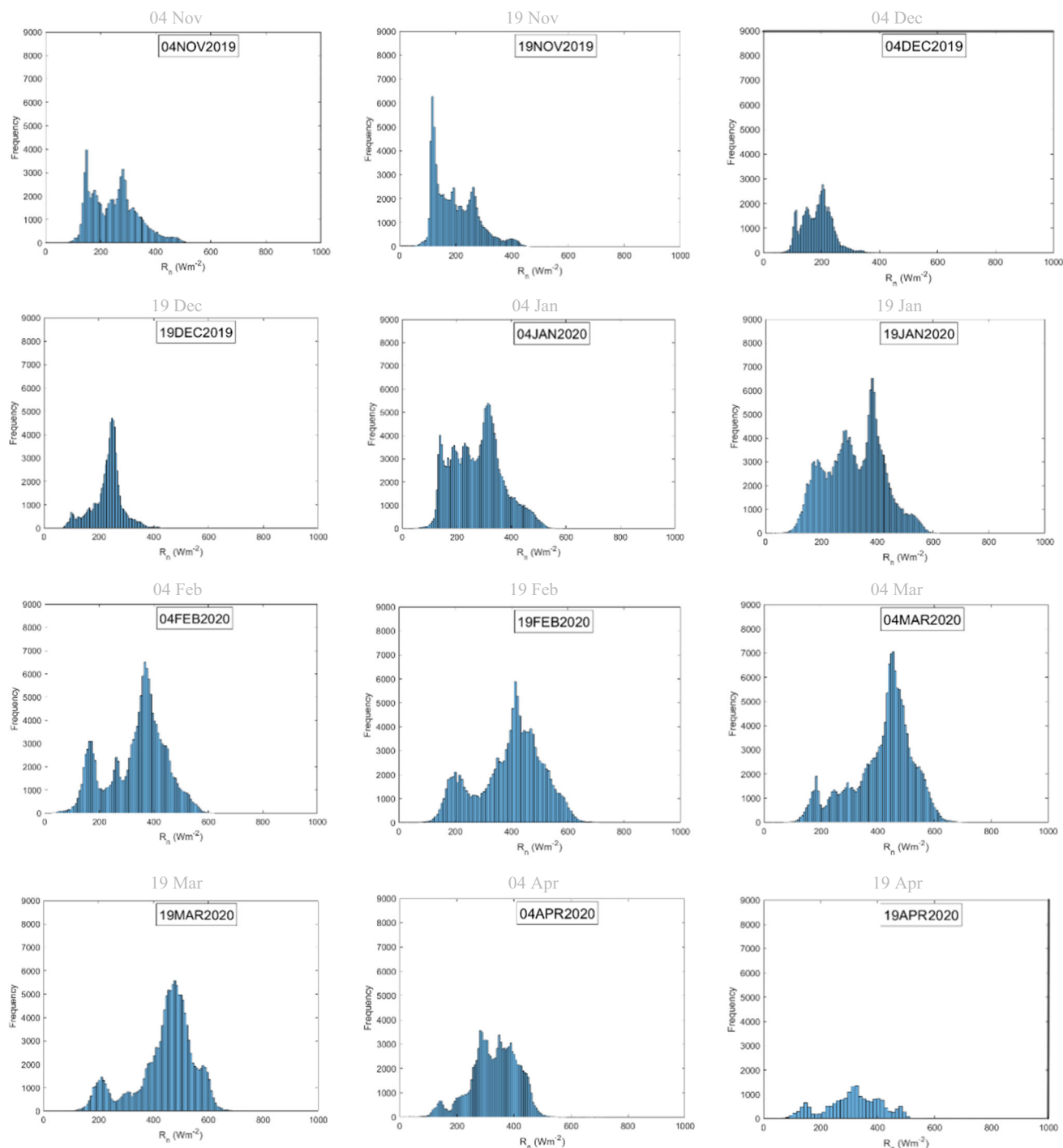


Figure 9. Histogram pattern of regional scale  $R_n$  estimates at 1530 IST on every fortnight between Nov 2019 and Apr 2020 over Indian landmass.

Ocean remain more active in January and February as compared to March or April (Dimri and Chevutri 2016). A skewness can be observed in the 4th and 19th January histograms, with two separate peaks. This might be due to the transition from winter to spring months and lower surface temperature. On 4th March,  $R_n$  showed least overcast conditions and also recorded the peak that was not observed in the

other histograms with maximum  $R_n$  around  $500 \text{ W m}^{-2}$ . The summary statistics showed a rise in the minimum and maximum satellite-based  $R_n$  due to the onset of spring over Indian landmass. Also, on the 19th of February, a sudden rise in the maximum  $R_n$  estimated from satellite was seen, but the pattern was skewed due to the availability of low number of cloudless pixels (only 61%) as against 4 February

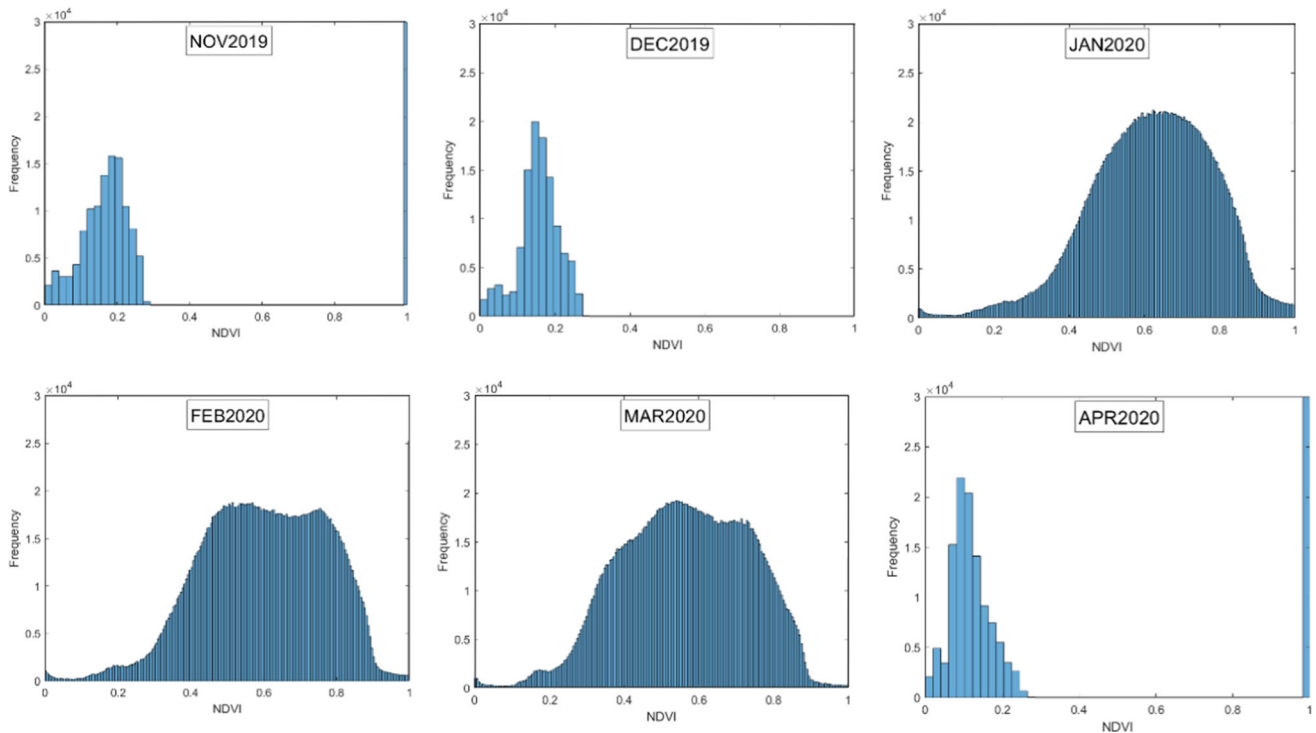


Figure 10. Monthly MODIS NDVI composite for the months of Jan, Feb, and Mar 2020.

(68%) or 4 March (73%) and lowest with 19 April (23%).

### 5. Conclusion

A model investigates and estimates  $R_n$  and its relevant fluxes derived from satellite measurements over the Indian landmass for daytime conditions under cloudless skies. The study provided a first-hand understanding of the flow and behaviour of radiation fluxes over Indian landmass. The current model and methodology can be used to estimate  $R_n$  over India only under cloudless conditions during daytime within 21% errors or *in situ* measured mean. Several uncertainties stemmed from scale-mismatch of inputs and measurement footprints as well as temporal scale of different model inputs could be reasons for the  $R_n$  errors. However, the present study showed that the modelled  $R_n$  estimates produced an order of accuracy similar to globally reported errors of satellite-based  $R_n$  estimates. The bias correction was found to reduce the errors of estimates to the tune of 5%. The regional  $R_n$  has shown reasonable variability from tetramodal to bio-modal distribution in three winter months. The current model can be used to estimate operational regional-scale cloudless-sky  $R_n$  estimates after validation for some more months and

over more *in situ* measurement sites. The generated  $R_n$  can be used as an input for generation of actual ET, assimilation in the land surface model of NWP and hydrological models.

### Acknowledgements

The authors would like to thank SAC (Space Application Centre), ISRO, Ahmedabad for providing datasets and infrastructure, to carry out this study. The authors would like to specially thank Dr G S Bhat, PI INCOMPASS campaign, CAOS, IISc Bangalore and Dr R Morrison CEH, Wallingford, UK for providing the *in-situ* measurements relevant to this study.

### Author statement

Dhwanilnath Gharekhan conducted the validations, analysis, developed the model, and drafted as well as edited the manuscript. Rahul Nigam and Devansh Desai did the field visits, data acquisition and manuscript editing. Bimal K Bhattacharya guided, supervised the analysis, model development as well as drafted and edited the manuscript. Parul R Patel assisted in editing the manuscript.

## Appendix

Table A1. *One-dimensional sensitivity analysis of  $R_n$  to land surface and meteorological inputs.*

Variable (s)	Mean	Deviation from mean	Percent deviation in $R_n$
$\alpha$	0.19	0.11–0.27	+12.6 to –8.6
$SW_{in}$	759.6 W m <sup>-2</sup>	531.7–987.5 W m <sup>-2</sup>	–21.1 to +22.3
$T_a$	305.3 K	296.3–314.3 K	–7.5 to +8.2
$T_s$	317.4 K	308.4–326.4 K	+8.1 to –8.9
$\varepsilon_s$	0.9	0.87–0.93	–2.3 to +2.2
$\varepsilon_a$	0.87	0.84–0.9	+2.6 to –2.6

Table A2. *Statistical performance of diurnal plots over Jaisalmer and Nawagam on selected dates of 2020.*

Location	Dates	No. of points	RMSE (W m <sup>-2</sup> )	PRMSE (%) of measured mean	$R^2$	MAE (%)
Jaisalmer	4 Nov	17	9.1	3.5	0.98	2.7
Jaisalmer	4 Dec	16	9.7	4.1	0.96	2.8
Jaisalmer	1 Jan	13	9.7	5.7	0.98	10.7
Jaisalmer	1 Feb	18	39.3	10.4	0.98	5.5
Jaisalmer	1 Mar	17	21.6	7.4	0.90	7.4
Jaisalmer	4 Apr	17	9.5	2.4	0.97	2.8
Nawagam	4 Nov	17	14.5	7.1	0.92	3.2
Nawagam	19 Dec	15	7.5	5.5	0.95	2.5
Nawagam	11 Jan	18	17.9	6.5	0.94	3.9
Nawagam	15 Feb	16	47.2	12.9	0.92	14.1
Nawagam	14 Mar	18	41.6	8.2	0.98	8.2
Nawagam	19 Apr	19	10.6	4.2	0.98	2.9
Samastipur	4 Nov	19	16.4	7.8	0.94	3.7
Samastipur	4 Dec	19	15.7	7.1	0.89	3.3
Samastipur	4 Jan	19	35.9	21.9	0.86	5.1
Samastipur	4 Feb	19	21.6	8.3	0.92	3.9
Samastipur	4 Mar	19	41.9	12.7	0.83	4.8
Samastipur	4 Apr	19	30.5	8.6	0.9	3.9

Table A3. *Summary statistics of regional-scale  $R_n$  estimates at 1530 IST on every fortnight between Jan and Mar 2020 over Indian landmass.*

Days	Minimum (W m <sup>-2</sup> )	Maximum (W m <sup>-2</sup> )	Mean (W m <sup>-2</sup> )	SD (W m <sup>-2</sup> )	Median (W m <sup>-2</sup> )
4 Nov	4	558	265	81	281
19 Nov	8	519	198	76	210
4 Dec	22	441	168	72	201
19 Dec	12	398	154	66	196
4 Jan	3	608	277	91	282
19 Jan	2	624	320	102	322
4 Feb	9	656	337	106	359
19 Feb	2	716	394	115	412
4 Mar	29	712	417	108	442
19 Mar	8	763	443	107	464
4 Apr	45	732	423	105	441
19 Apr	51	598	342	103	312

SD: Standard deviation.

## References

- Abramowitz G, Pouyanne L and Ajami H 2012 On the information content of surface meteorology for downward atmospheric long-wave radiation synthesis; *Geophys. Res. Lett.* **39**(4).
- Backeberg B, Penven P and Rouault M 2012 Impact of intensified Indian Ocean Winds on mesoscale variability in the Agulhas system; *Nat. Clim. Change* **2**(8) 608–612.
- Bastiaanssen W G 1995 Regionalization of surface flux densities and moisture indicators in composite terrain; Wageningen (The Netherlands): Wageningen Agricultural University, Wageningen.
- Bhattacharya B K, Dutt C and Parihar J 2009 INSAT Uplinked Agromet Station: A scientific tool with a network of automated micrometeorological measurements for soil-canopy-atmosphere feedback studies; *ISPRS Archives XXXVIII-8/W3 Workshop Proceedings: Impact of Climate Change on Agriculture*, pp. 72–77.
- Bojinski S, Verstraete M, Peterson T C, Richter C, Simmons A and Zemp M 2014 The concept of essential climate variables in support of climate research, application and policy; *Am. Meteorol. Soc.* **95**(9) 1431–1443.
- Cammalleri C, Anderson M C, Gao F, Hain C R and Kustas W P 2013 A data fusion approach for mapping daily evapotranspiration at field scale; *Water Resour. Res.* **49**(8) 4672–4686.
- Carmona F, Rivas R and Caselles V 2014 Estimation of daytime downward longwave radiation under clear and cloudy skies conditions over a sub-humid region; *Theor. Appl. Climatol.* **115**(1) 281–295.
- (CDS) C C 2017 Copernicus Climate Change Service (C3S) 2017: ERA5: Fifth generation of ECMWF atmospheric reanalyses of the global climate; <https://cds.climate.copernicus.eu/cdsapp#!/home>.
- Chattopadhyay N, Sahai A K, Guhathakurta P, Dutta S, Srivastava A K, Attri S D and Chandras S 2019 Impact of observed climate change on the classification of agroclimatic zones in India; *Curr. Sci.* **117**(3) 480–486.
- Dewitte S and Clerbaux N 2017 Measurement of the earth radiation budget at the top of the atmosphere: A review; *Remote Sens.* **9**(1143) 1–13.
- Dimri A P and Chevuturi A 2016 Western disturbances: An Indian meteorological perspective (1st edn); Springer, New Delhi.
- García M, Villagarcía L, Contreras S, Domingo F and Puigdefábregas J 2007 Comparison of three operative models for estimating the surface water deficit using ASTER reflective and thermal data; *Sensors* **7** 860–883.
- Gharekhan D, Bhattacharya B K, Desai D and Patel P R 2021 Neural network-based approach for estimation of downwelling longwave radiation flux under cloudy-sky conditions; *J. Appl. Remote Sens.* **15**(2) 1–25.
- Ghosh S 1991 Agro-climatic zone specific research: Indian perspective under NARP (1st edn); ICAR, New Delhi.
- Hartmann D L 2016 *Global Physical Climatology* (2nd edn); Seattle, WA, USA: Elsevier Science Publishers.
- Hersbach H, Bell B, Berrisford P, Hirahara S, Horányi A and Muñoz-Sabater J 2020 The ERA5 global reanalysis; *Quart. J. Roy. Meteorol. Soc.* **146**(730) 1999–2049.
- ISRO 2019 July 19 INSAT derived Insolation; <https://mosdac.gov.in/catalog/doi/150>.
- Jones J W, Antle J M, Basso B, Boote K J, Godfray R T, Herrero M and Wheeler T 2017 Toward a new generation of agricultural system data, models and knowledge products: State of agricultural systems science; *Agric. Syst.* **155** 269–288.
- Kalnay E, Kanamitsu M, Kistler R, Collins W, Gandin D D, Iredell M and Jose D 1996 The NCEP/NCAR 40-year reanalysis project; *Bull. Am. Meteorol. Soc.* **77**(3) 437–472.
- Kesarwani A, Kaur A S, Kaur M and Vohra P S 2018 Performance analysis of FSO link under different conditions of fog in Delhi, India; *2018 2nd IEEE International Conference on Power Electronics, Intelligent Control and Energy Systems (ICPEICES)*.
- Kumar P, Ojha S P, Singh R, Kishtawal C M and Pal P K 2016 Performance of weather research and forecasting model with variable horizontal resolution; *Theor. Appl. Climatol.* **126**(3) 705–713.
- Kumar P, Shukla M V, Thapliyal P K, Bisht J H and Pal P K 2012 Evaluation of upper tropospheric humidity from NCEP analysis and WRF Model Forecast with Kalpana observation during Indian summer monsoon 2010; *Meteorol. Appl.* **19**(2) 152–160.
- Kumar P, Singh R, Joshi P C and Pal P K 2011 Impact of additional surface observation network on short-range weather forecast during summer monsoon 2008 over Indian subcontinent; *J. Earth Syst. Sci.* **120**(1) 53–64.
- Long D, Gao Y and Singh V 2010 Estimation of daily average net radiation from MODIS data and DEM over the Baiyangdian watershed in North China for clear sky days; *J. Hydrol.* **388**(3) 217–233.
- Masoom A, Kosmopoulos P, Bansal A and Kazadzis S 2020 Solar energy estimations in India using remote sensing technologies and validation with sun photometers in urban areas; *Remote Sens.* **12**(254) 1–25.
- McCreary J P, Han W, Shankar D and Shetye S R 1996 Dynamics of the East India coastal current: 2. Numerical solutions; *JGR Oceans* **101**(C6) 13,993–14,010.
- Mishra M K, Rastogi G and Chauhan P 2014 Operational retrieval of aerosol optical depth over Indian subcontinent and Indian Ocean using INSAT3D/IMAGER and product validation; Hyderabad, India: *The International Archives of the Photogrammetry, Remote Sensing and Spatial Information Sciences, Volume XL-8, 2014, ISPRS Technical Commission VIII Symposium, 09–12 Dec 2014*.
- Moghim S and Bras R L 2017 Bias correction of climate modelled temperature and precipitation using artificial neural networks; *J. Hydrometeorol.* **18**(7) 1867–1884.
- NASA and Frazier S 2019 MODIS land surface temperature and emissivity (MOD11); <https://modis.gsfc.nasa.gov/data/dataproduct/mod11.php>.
- NASA and Schaaf C 2019 MCD43C3v006 - MODIS/Terra and Aqua BRDF/Albedo Albedo Daily L3 Global 0.05 Deg CMG; <https://lpdaac.usgs.gov/products/mcd43c3v006/>.
- Nigam R, Bhattacharya B K, Vyas S and Oza M P 2014 Retrieval of wheat leaf area index from AWiFS multispectral data using canopy radiative transfer simulations; *Int. J. Appl. Earth Obs. Geoinfo.* **32** 173–185.
- Pandya M R, Shah D B, Trivedi H J, Panigrahy S, Parihar J S and Kirankumar A S 2011 Evaluation of split-window algorithms for retrieving land surface temperature from the INSAT-3D imager observations; *Vayu Mand.* **37**(1) 31–37.

- Qian Y, Long C N, Wang H, Comstock J M, McFarlane S A and Xie S 2012 Evaluation of cloud fraction and its radiative effect simulated by IPCC AR4 global models against ARM surface observations; *Atmos. Chem. Phys.* **12**(4) 1785–1810.
- Renzullo L J, Barrett D J, Marks A S, Hill M J, Guerschman J P and Mu Q 2008 Multi-sensor model-data fusion for estimation of hydrologic and energy flux parameters; *Res. Sens. Environ.* **112**(4) 1306–1319.
- Roelofs G J 2012 Aerosol lifetime and climate change; *Atmos. Chem. Phys. Discuss.* **12**(7) 16,493–16,514.
- Rubel F and Kottek M 2011 Comments on: “The thermal zones of the Earth” by Wladimir Koppen (1884); *Meteo. Zeit.* **20**(5) 361–365.
- Soriano E, Mediero L and Garijo C 2019 Selection of bias correction methods to assess the impact of climate change on flood frequency curves; *Water* **11**(2266) 1–16.
- Turner A G, Bhat G S, Martin G M, Parker D J, Taylor C M, Mitra A K and Wille P D 2019 Interaction of convective organization with monsoon precipitation, atmosphere, surface and sea: The 2016 INCOMPASS field campaign in India; *Quart. J. Roy. Meteorol. Soc.* **146**(731) 2828–2852.
- Verma M, Fisher J B, Mallick K, Ryu Y, Kobayashi H, Guillaume A and Cescatti A 2016 Global surface net-radiation at 5 km from MODIS Terra; *Remote Sens.* **8**(739) 1–20.
- Wei W, Zhi-jie L, Yue Z and Xiao-qing G 2019 The application of data fusion method in the analysis of ocean and meteorology observation data; *Int. J. Hydrol.* **3**(3) 205–208.
- Wei Z, Lee X, Wen X and Xiao W 2018 Evapotranspiration partitioning for three agro-ecosystems with contrasting moisture conditions: A comparison of an isotope method and a two-source model calculation; *Agric. For. Meteorol.* **252** 296–310.
- Wild M, Hakuba M Z, Folini D, Dörig O P, Schär C, Kato S and Long C N 2019 The cloud-free global energy balance and inferred cloud radiative effects: An assessment based on direct observations and climate models; *Clim. Dyn.* **52**(7) 4787–4812.
- Wu B, Liu S, Zhu W, Yan N, Xing Q and Tan S 2017 An improved approach for estimating daily net radiation over the Heihe River Basin; *Sensors* **17**(86) 1–18.
- Yang Y and Shang S 2013 A hybrid dual-source scheme and trapezoid framework-based evapotranspiration model (HTEM) using satellite images: Algorithm and model test; *JGR Atmos.* **118**(5) 2284–2300.
- Yoon J, Burrows J P, Vountas M, Hoyningen-Huene W V, Chang D Y, Richter A and Hilboll A 2014 Changes in atmospheric aerosol loading retrieved from space-based measurements during the past decade; *Atmos. Chem. Phys.* **14**(13) 6881–6902.
- Zhang J, Zhao L, Deng S, Xu W and Zhan Y 2017 A critical review of the models used to estimate solar radiation; *Renew. Sustain. Energy Rev.* **70** 314–329.
- Zhang W, Jin H, Bian J, Zhang Z, Lei G and Huang C 2013 An enhanced spatial and temporal data fusion model for fusing landsat and MODIS surface reflectance to generate high temporal Landsat-like data; *Remote Sens.* **5**(10) 5346–5368.
- Zonen K 2019 CNR4 Net Radiometer; <https://www.kippzonen.com/Product/85/CNR4-Net-Radiometer>.

Corresponding editor: T NARAYANA RAO